

Multi-parametric field experiment links explosive activity and persistent degassing at Stromboli

Simon Thivet, Andrew J L Harris, Lucia Gurioli, Philipson Bani, Talfan Barnie, Maxime Bombrun, Emanuele Marchetti

▶ **To cite this version:**

Simon Thivet, Andrew J L Harris, Lucia Gurioli, Philipson Bani, Talfan Barnie, et al.. Multi-parametric field experiment links explosive activity and persistent degassing at Stromboli. 2021. hal-03240733

HAL Id: hal-03240733
https://uca.hal.science/hal-03240733

Preprint submitted on 28 May 2021

HAL is a multi-disciplinary open access archive for the deposit and dissemination of scientific research documents, whether they are published or not. The documents may come from teaching and research institutions in France or abroad, or from public or private research centers.

L'archive ouverte pluridisciplinaire **HAL**, est destinée au dépôt et à la diffusion de documents scientifiques de niveau recherche, publiés ou non, émanant des établissements d'enseignement et de recherche français ou étrangers, des laboratoires publics ou privés.



Distributed under a Creative Commons Attribution 4.0 International License

Multi-parametric field experiment links explosive activity and persistent degassing at Stromboli

Simon Thivet[1,2*], Andrew J. L. Harris[1], Lucia Gurioli[1], Philipson Bani[1], Talfan Barnie[3], Maxime Bombrun[4], Emanuele Marchetti[5]

[1] Laboratoire Magmas et Volcans, Université Clermont Auvergne - CNRS - IRD, OPGC, Aubière, France
[2] Department of Earth and Environmental Sciences, Ludwig-Maximilians-Universität München, Germany
[3] Nordic Volcanological Center, Institute of Earth Science, University of Iceland, Reykjavik, Iceland

[4] Department of Information Technology, Division of Visual Information and Interaction, and Science for Life Laboratory, Uppsala University, Sweden
[5] Dipartimento di Scienze della Terra, Università degli Studi di Firenze, Firenze, Italy

*** Correspondence:**
Corresponding Author email:
simon.thivet@lmu.de

Keywords: Ash characterization; explosive degassing; particle size distribution; persistent degassing; pyroclast mass flux; real-time monitoring; Strombolian explosions

Abstract

Visually unattainable magmatic processes in volcanic conduits, such as degassing, are closely linked to eruptive styles at the surface, but their roles are not completely identified and understood. To gain insights, a multi-parametric experiment at Stromboli volcano (Aeolian Islands, Italy) was installed in July 2016 focusing on the normal explosive activity and persistent degassing. During this experiment, gas-dominated (type 0) and particle-loaded (type 1) explosions, already defined by other studies, were clearly identified. A FLIR thermal camera, an UV SO_2 camera and a scanning DOAS were deployed to record pyroclast and SO_2 masses emitted during individual explosions, as well as persistent SO_2 fluxes, respectively. An ASHER instrument was also deployed in order to collect ash fallouts and to measure the grain size distribution of the samples. SO_2 measurements confirm that persistent degassing was far greater than that emitted during the explosions. Further, we found that the data could be characterized by two periods. In the first period (25-27 July), activity was mainly characterized by type 0 explosions, characterized by high velocity jets. Pyroclast mass fluxes were relatively low (280 kg/event on average), while persistent SO_2 fluxes were high (274 t/d on average). In the second period (29-30 July), activity was mainly characterized by type 1 explosions, characterized by low velocity jets. Pyroclast mass fluxes were almost ten times higher (2400 kg/event on average), while persistent gas fluxes were significantly lower (82 t/d on average). Ash characterization also indicates that type 0 explosions fragments were characterized by a larger proportion of non-juvenile material compared to type 1 explosions fragments. This week-long field experiment suggests that, at least within short time periods, Stromboli's type 1 explosions can be associated with low levels of degassing and the mass of particles accompanying such explosive events depends on the volume of a degassed magma cap sitting at the head of the magma column. This could make the classic particle-loaded explosions of Stromboli an aside from the true eruptive state of the volcano. Instead, gas-dominated explosions can be associated with high

levels of degassing and are indicative of a highly-charged (with gas) system. We thus suggest that relatively deep magmatic processes, such as persistent degassing and slug formation can rapidly influence the superficial behavior of the eruptive conduit, modulating the presence or absence of degassed magma at the explosion/fragmentation level.

1 Introduction

Characterizing physical processes that drive explosive eruptions, as well as post-fragmentation transport and deposition of the eruptive products, are mandatory if we are to understand the associated volcanic hazards and risks (e.g. Barberi et al. 1993; Nave et al. 2010; Rosi et al. 2013). A number of modern geophysical and sampling techniques allow to define key eruptive parameters that inform on those physical processes. These include gas flux and composition (e.g. Aiuppa et al. 2009; Burton et al. 2009; Barnie et al. 2015; Delle Donne et al. 2017; Pering et al. 2020), pyroclast dynamics and size distributions (e.g. Patrick et al. 2007; Harris et al. 2012; Taddeucci et al. 2012), and the physical and chemical characteristics of the eruptive products (e.g. D'Oriano et al. 2010; Pioli et al. 2014; Gurioli et al. 2015). When measured together, these parameters can allow well-constrained models to be built for the physical processes operating before and at fragmentation, as well as during particle transport and deposition. We therefore implemented an experimental multi-parametric monitoring network at Stromboli volcano (Italy) to synchronously measure all of these parameters so as to constrain the transport and deposition characteristics of Stromboli's explosive activity, and hence understand the magma ascent and fragmentation conditions that drive the activity.

Stromboli has been characterized by mildly explosive, "Strombolian" activity for at least 2000 years (Mercalli 1907; Barberi et al. 1993; Rosi et al. 2000), from a stable system of three summit craters (Washington 1917; Harris and Ripepe 2007a; Fig. 1): northeast (NE), central (C) and southwest (SW). This makes Stromboli an ideal "natural laboratory" (Harris and Ripepe 2007a) where we can study explosive volcanism and associated eruptive processes (Taddeucci et al. 2015) that can be tested at, transferred to and adapted for other systems characterized by "Strombolian" activity, such as Shishaldin, Erebus, Yasur (e.g. Vergniolle et al. 2004; Johnson et al. 2008; Gerst et al. 2013; Simons et al. 2020a; 2020b). The "normal" Strombolian activity on which we focus here is characterized by intermittent "mildly explosive" activity (Barberi et al. 1993) that typically involves 10^2 to 10^3 kg of material (Harris et al. 2013) in repeated emissions of gas, bombs, lapilli and ash in events that last a few to tens of seconds, (Rosi et al. 2013; Houghton et al. 2016). Normal Strombolian activity, and its associated geophysical (seismic and infrasonic) signals, is classically explained by the generation, ascent and bursting of large gas bubbles (slugs) at the free surface (e.g. Blackburn et al. 1976; Jaupart and Vergniolle 1988; 1989; Ntepe and Dorel 1990; Braun and Ripepe 1993; Vergniolle and Brandeis 1994; 1996; Parfitt and Wilson 1995; Chouet et al. 1999; 2003). However, in-spite of the persistence of activity and commonality of source process, normal Strombolian activity is highly variable in style, and three different types of normal explosions have been identified on the basis of plume type, componentry and ascent dynamics:

(i) type 0 explosions are gas-dominated, involving high velocity jets moving at velocities of hundreds of meters per second, but only involving a few particles (Goto et al. 2014; Leduc et al. 2015; Gaudin et al. 2017).

(ii) type 1 explosions are dominated by lapilli and bomb rich emissions (Patrick et al. 2007), dominated by particles that follow ballistic trajectories (Chouet et al. 1974) and involving masses of the order of 10^3 kg (Harris et al. 2013).

(iii) type 2 explosions produce ash-rich plumes (Patrick et al. 2007), where plumes follow convective ascent dynamics (Fig. 2).

These different plume types can be identified at most Strombolian systems, such as Yasur and Etna (Gaudin et al. 2017; Simons et al. 2020b), and have been increasingly associated with bubble bursting through a more (for type 1/2) or less (for type 0) "capped" surface; the cap comprising a layer of high-viscosity, degassed magma (Lautze and Houghton 2005; 2007; Gurioli et al. 2014; Del Bello et al. 2015; Leduc et al. 2015; Capponi et al. 2016; Suckale et al. 2016; Oppenheimer et al. 2020) that can be involved also in more energetic activity (Caracciolo et al. 2021).

Between normal Strombolian explosions, activity is dominated by persistent degassing (Francis et al. 1993; Allard et al. 1994; Allard 1997; Harris and Stevenson 1997; Pering et al. 2016) and puffing, characterized by continuous, bursts of gas in a continuous train of "explosions" that are weakly (0.1 bar) over-pressured (Ripepe and Gordeev 1999; Harris and Ripepe 2007b). Again, this style of activity has been identified as common to many "Strombolian" systems, including Etna, Villarrica and Masaya (Gresta et al. 2004; Branan et al. 2008; Gurioli et al. 2008). Within this mixed (Strombolian explosions and persistent degassing) activity regime, outstanding questions are (i) related to the roles of, and relations between, these two co-existing activity types in driving changes in activity level and style, and (ii) related to the underlying (deep and shallow conduit system) physical processes. In setting up experiments to answer these questions, we can improve definition and design of monitoring networks, as well as processing, integration and interpretation of the data output, so as to better assess hazard types and risk levels at the associated system (e.g., Calvari et al. 2005; Ripepe et al 2005; Bertolaso et al. 2009).

Hence, the aim of our study was to monitor and track, over a few days, the normal Strombolian and persistent degassing activity of Stromboli by (i) observing the explosive activity, (ii) recording synchronous data concerning the solid (pyroclast) and gas (persistent and explosive) emissions of Stromboli volcano, and (iii) collecting and characterizing ash fallout samples. Combining a carefully designed and deployed experiment, involving multiple field-based remote sensing measurements and samplings with post-eruptive laboratory analysis, is crucial to bridge the gap between visually unattainable magmatic processes (i.e. conduit conditions) and their superficial manifestations (i.e. explosion style, pyroclast mass emission, particle size distribution, gas flux) as recordable using multispectral measurements spanning laser, ultraviolet and infrared. More specifically, we aim to answer the follow open questions:

(i) Is there any correlation between persistent and/or explosive gas and solid fluxes emitted by the normal Strombolian explosions?

(ii) Does ash characterization help in understanding the fragmentation mechanisms of the associated measured explosions?

(iii) What are the magmatic processes at the origin of the transitions observed in the eruptive styles, especially between type 0 and type 1 explosions?

Most importantly, we show how multi-parametric measurements, involving traditional and modern remote sensing technologies, can be deployed and coupled to monitor, track and understand activity levels at active persistently degassing Strombolian systems.

2 Methods

This multi-parametric field experiment involved deployment of three ground-based remote sensing instruments (Fig. 1): a high speed thermal FLIR (Forward Looking Infra-Red) camera, a UV (Ultra-Violet) camera and a scanning DOAS (Differential Optical Absorption Spectroscopy); plus a new instrument capable of remotely sampling active fall out in real time using a laser barrier, an ASHER (ASH collector and sizER).

These instruments were deployed around the active summit craters and on the lower flanks for a six-day-long period between July 25 and 30, 2016. All instruments were constantly geo-located and synchronized at the same local time in order to get a synchronized and exploitable dataset over the entire experiment duration. In addition, observational logs were kept during all summit visits detailing the time, location and type of each explosion (as summarized in Table S1).

2.1. Measurement strategy and instrument layout

Normal explosions at Stromboli are generally understood to be sourced by the generation and ascent of a large gas bubble (or slug), generated at some depth, which then ascends to burst at the free-surface to cause fragmentation of the magma resident in the conduit (e.g., Chouet et al., 1999; 2003; Burton et al. 2007a). After fragmentation, the mixture of gas and particles ascends the conduit to be released from the vent as an explosive emission (Ripepe et al. 2001; 2002). Thereafter, evolution of a normal explosive event at Stromboli follows five chronologically ordered steps (Fig. 2a). The first is emission of the mixture of gas and particles from the vent as a jet (step 1 in Fig. 2a), followed by initial plume ascent and development of a rooted thermal (step 2 in Fig. 2a). In steps three and four, bombs, blocks and larger lapilli following ballistic trajectories begin to land proximal to the vent (step 3 in Fig. 2a), and a cloud of finer particles and gas detaches to drift in the wind (step 4 in Fig. 2a). Finally, finer particles (ash) falls out from the cloud at distal locations (step 5 in Fig. 2a). Each step can thus be sampled using different remote sensing and real-time sampling approaches to parameterize various components of the emission. These span the at-vent conditions in terms of exit velocity and particle size distribution to distal fall out conditions in terms of ash mass and componentry. We thus designed our experiment to constrain (in terms of gas/particle masses and particle sizes) the mixture comprising the plume, as well as the dynamics (velocities and fluxes) and nature (chemistry and texture) of the particles; all constraints that can be used to inform on the conduit conditions at the time of fragmentation. As sketched in Figure 2b, the network configuration was thus designed to use each of the steps to extract data to inform on the fullest possible range of parameters as follows:

(i) High speed thermal video of the mixture leaving the vent (step 1 in Fig. 2b) allows to measure the pyroclast mass, the particle size distributions and the vent-leaving velocities of the particles (cf. section 2.2).

(ii) The UV SO_2 camera then allows measurement of the SO_2 mass within the plume (step 2 in Fig. 2b), and with the thermal camera data allows for pyroclast/gas mass ratio to be characterized (cf. section 2.3).

(iii) Vent-proximal fallout of ballistics (step 3 in Fig. 2b) can be sampled to inform on the texture and chemistry of the conduit magma if conditions are ideal (e.g. Lautze and Houghton 2008; Gurioli et al. 2014; Leduc et al. 2015); however the geometry of the crater meant that this was not possible during our deployment.

(iv) The SO_2 flux associated with the gas-rich drifting clould (step 4 in Fig. 2b), as well as persistent degassing and puffing between explosions, can be measured with the DOAS instrument (cf. section 2.4).

(v) Finally, sedimentation of particles from the drifting cloud (step 5 in Fig. 2b) can be sampled and characterized in terms of grain size and terminal velocity by an ASHER instrument (cf. section 2.5). Sample return then allows textural, chemical and componentry analysis.

When tracked through time, this configuration allows to link changes of the emission properties to conduit conditions as witnessed by, for example, changes in particle mass, particle size distribution, componentry and/or gas flux, to changes in the eruptive style and the persistent gas flux. We next detail the new elements of our integrated, ground-based remote sensing array, i.e., the thermal camera, SO_2 camera, DOAS and ASHER, and the data processing steps.

2.2. Forward Looking Infra-Red (FLIR) camera: insights into pyroclast mass emission

A FLIR 655sc camera (Fig. 3a) was used to derive the total pyroclast masses ejected during individual explosions using the particle tracking algorithm and particle parameter (velocity, dimensions, shape, volume and mass) calculation procedures described in Bombrun et al. (2014; 2015). This procedure allows detection of all emitted particles and removal of background pixels, which may contain hot particles lying on the ground as deposited during previous explosions. Pixel dimensions are computed, the long and short axis of each particle retrieved, and particle volume is calculated by assuming rotational symmetry about the long axis. The mass is calculated by multiplying the volume by an appropriate density: two densities from samples collected at Stromboli between 2008 and 2011 were defined so that the conversion depending on particle size. While the density distribution for bombs (> 64 mm, following the Schmid 1981 nomenclature) is tight with a mean and standard deviation of 1.8 ± 0.2 g/cm^3, that for large lapilli (between 50 and 64 mm) forms a cluster with a mean and standard deviation of 1.0 ± 0.2 g/cm^3 (Gurioli et al. 2013; 2014; Bombrun et al. 2015). These two values are used for the size-dependent conversion to mass, which gives an error on the final total mass of ±10 %.

The focal plane array of the FLIR camera is composed of uncooled microbolometers sensitive between 7 and 14 µm. The camera was installed viewing into the South West (SW) crater from the Pizzo Sopra la Fossa (PSF) over a distance from the vent of around 250 m (Fig. 1b). The camera was equipped with a 3.6× magnification lens and acquired 640 × 120 images at 200 frames per second for a rectangular zone immediately above the vent (see Bombrun et al. (2014; 2015) for targeting configuration). The focal length was 88.9 mm and the instantaneous field of view was 0.19 mrad, giving for the line of sight tilt angle of -30°, a pixel size of 5 cm.

2.3. Ultra-Violet (UV) SO_2 camera: insights into explosive SO_2 emission

Explosive SO_2 masses (i.e. gas emitted by an explosion) were measured using an UV SO_2 camera system following Barnie et al. (2015). Our UV SO_2 camera system consists of two QSI-620s UV cameras and an Ocean Optics USB2000+ UV spectrometer (Fig. 3b). The cameras are mounted with 25 mm f2.8 Universe Optics quartz lenses, giving a Field Of View (FOV) of 23° by 17.25°. Both lenses are fitted with Asahi Spectra 10 nm bandpass filters in front of the lens, one at 310 nm (SO_2 absorption) and one at 330 nm (no SO_2 absorption). The spectrometer is connected to an Ocean Optics 74-UV 10 mm f2 telescope oriented within the FOV of the cameras with an FOV of 5.7 °.

The UV SO_2 camera was set up just next to the FLIR, also viewing into the SW crater (Fig. 1b), and images and spectra were collected every 5 s. Each image was subject to a flat field correction using dark current and clear sky images and corrected for incidence angle wavelength shift effects (Smekens et al. 2015). Each corrected 330/310 nm image pair was then aligned using the phase correlation technique (Kuglin and Hines 1975; De Castro and Morandi 1987) and used to calculate an Apparent Absorption (AA) image. The location of the spectrometer FOV within the camera FOV was found by simulating camera AA for each spectrum, interpolating the spectral AA time series to the camera acquisition times, smoothing the camera AA time series spatially on a length scale of the spectrometer FOV, and finding the location within the camera FOV that gave the highest correlation coefficient between smoothed camera AA and interpolated spectral AA. The total column amount of SO_2 in ppmm (parts per million meters) was found using the iFit technique (Barnie et al. 2015; Burton and Sawyer 2016). The calibration relationship was found by fitting the camera AA time series at the center of the spectrometer FOV with the spectral ppmm interpolated to the image acquisition times. This relationship was then used to calibrate all the AA images to ppmm. Images containing explosions were identified, the explosion plumes digitized and the total area and mean ppmm values calculated, and the total SO_2 mass derived using the ideal gas law.

2.4. Differential Optical Absorption Spectroscopy (DOAS): insights into persistent SO_2 degassing

During the six days of field recording we carried out DOAS measurements in a stationary scanning mode at three different locations. We used locations to capture best the total SO_2 persistent flux from the three summit craters (Fig. 1b), so measurement sites were selected depending on wind direction and velocity so that the whole plume was scanned (Williams-Jones et al. 2006). On some days, measurements at the summit were difficult due to wind conditions that caused the gas to pond as a "vog" (Businger et al. 2015) over the Pizzo Sopra la Fossa and the upper slopes of the Sciara del Fuoco. Accordingly, on July 25 and 27, combined vertical scanning measurements were performed at about 400 m from the active craters (870 m above sea level). On July 26 and 30, vertical scanning was carried out 2 km northeast of the crater (65 m above sea level). Finally, on July 28 and 29 the system was positioned at Pizzo Sopra la Fossa, around 150 m from the eastern crater rim (920 m above sea level), but performing sub-horizontal scanning. The spectrometer used was an Ocean Optics USB2000+ with a spectra range of 290-440 nm and a spectral resolution of 0.5 FWHM (Fig. 3c). The SO_2 column amounts in ppmm were retrieved using DOAS calibration and standard analysis procedures (Platt and Stutz 2008). Reference spectra included in the non-linear fit were obtained by convolving high resolution SO_2 and O_3 cross sections with the instrument line shape (Voigt et al. 2001; Bogumil et al. 2003). A Fraunhofer reference spectrum and ring spectrum were also included in the fit. The total column amount of the plume cross section was then multiplied by the plume velocity to derive the SO_2 emission rates. In this work, for the vertical scanning, the plume dispersal speed was considered equivalent to the wind velocity, obtained from a hand-held anemometer. For the sub-horizon scanning, the plume ascent speeds were obtained using the thermal infrared camera and used as the velocity.

2.5. ASH collector and sizER (ASHER) and laboratory ash characterization: insights into grain size distribution and componentry

Characterizing the eruptive products, especially ash (particle diameter < 2 mm following the Schmid 1981 nomenclature), is also a key to understand the eruptive processes involved in generating a Strombolian explosion. In order to collect and characterize the ash particles related to the measured explosions, an optical barrier (ASHER, Fig. 3d) was deployed at two different locations around the summit craters (Fig. 1b). Between July 25 and 28, it was installed at Pizzo Sopra la Fossa (at 915 m above sea level), while on July 29 it was installed closer to the SW crater (at 855 m above sea level).

The ASHER optical barrier consists of a laser and a receiver which detects particles when they cross the laser beam: a 90CM-M140 laser (wavelength 635 ± 5 nm) is used to produce the linear (30 x 1 mm) laser beam. Operating at a sampling rate of 30 kHz, particles are detected from laser obscuration with the amplitude and duration of the absorption peak being representative of the particle diameter and terminal velocity, respectively. Ash particles are collected in a container below the laser beam. ASHER measurements are performed for 10 seconds every 30 seconds, allowing near-real time analysis of Grain Size Distribution (GSD). For this, the number of detected particles is provided and divided into 13 bins of diameter spanning from Φ >= -1.5 (2800 μm) to Φ <= 3.5 (90 μm), with a step of 0.5 Φ, thus covering the coarse ash fractions.

Exploitable ash samples, emitted from the SW crater, were then analyzed. Laboratory sieving was performed to isolate the different grain size bins with a step of 0.5 Φ and to compare with the syn-eruptive ASHER data. Selected ash fractions were prepared in polished epoxy grain mounts. Componentry analysis was performed on the 180-250 μm grain size bin, based on Back-Scattered Electron (BSE) mosaic images acquired with the Cameca SxFiveTactis Electon Probe Micro Analyzer (EPMA). In parallel, in-situ glass and crystal analysis were performed using the same EPMA instrument, with a 15 kV acceleration voltage and a focused spot size (1 μm) for crystals and a spot diameter of 20 μm for the glass. Ash morphology measurements were also carried out using the automatized morpho-grainsizer Malvern Morphologi G3, following the procedure

described in Thivet et al. (2020a; 2020b). This instrument allows measurement of the Apparent Projected shape of ASH (APASH) on hundreds of ash particles, listing several shape parameters (described in Leibrandt and Le Pennec 2015) for each analyzed particle. Roughness (solidity, which corresponds to the area of the projected ash shape divided by the convex hull area of the projected ash shape) and morphological (convexity, which corresponds to the convex hull perimeter of the projected ash shape divided by the perimeter of the projected ash shape) parameters are used to identify shape variations between the ash samples. These measurements were performed on the same grain size bin as the componentry analysis (i.e. 180-250 µm).

3 Results

3.1. Field observations

Summit-based observations made between 25 July and 30 July 2016 permitted to identify two significantly different periods in terms of explosion types (Fig. 4a): the first between 25 and 27 July being dominated by Type 0 explosions, and the second between 29 and 30 July being dominated by Type 1 events (a transition period can also be identified on 28 July being dominated by Type 0 explosions but with the progressive occurrence of type 1 explosions). As shown by our field experiments results, these two main periods were also marked by systematic changes in particle velocities, numbers, and masses (Fig. 4b), as well as SO_2 degassing (Fig. 4c). All the field experiments results are displayed in Figure 4d and are further detailed in the following results sections. Weather conditions were relatively stable during all field measurements, with low (typically 3.5 m/s) wind speed, stable direction (generally SSW) and no precipitation, but sometimes with summit cloud cover (all observations are reported in Table S1).

During the first period, between 25 and 27 July, an average of five explosions per hour was measured. These explosions were mainly from vents in the SW crater and were characterized by gas-dominated type 0 explosions, which accounted for 80 % of the total recorded explosions. These explosions involved gas-roars, with no or very few particles heard landing. On the 28 July, loads of lapilli (particle diameter between 2 and 64 mm according to the Schmid 1981 nomenclature) slightly increased. The 20 % remaining events were silent type 2 (four 2a and four 2b) explosions, both within SW and North East (NE) craters. These type 2 explosions produced thermals that rose up to around 300 m above the craters.

During the second period, on 29 and 30 July, a total of 27 events were counted over an observation period of five and a half hours, giving a frequency of around five explosions per hour on average. Again, these explosions were mainly occurring in the SW crater (with very scarce events in the C and NE craters), but were now characterized by particle-loaded type 1 explosions which accounted for 90 % of the events. These explosions involved bomb-loaded ejections, which fell back into the crater or being sent out onto the Sciara del Fuoco to the north, prohibiting sampling. The 10 % remaining events were silent type 2b explosions that occurred in the NE crater.

3.2. Pyroclasts mass emission

Three type 0 explosions during the first period were fully recorded with the FLIR camera on the 27 July. The first recorded explosion yields a mass of just 5 kg of pyroclast distributed between 11 particles. The two other recorded explosions are represented through the FLIR image sequences shown in Figures 5a and 5b, corresponding respectively to the second (total pyroclast mass of 645 kg with 456 detected particles) and the third (total pyroclast mass of 190 kg with 64 detected particles) explosions recorded during this day. For all of these type 0 explosions, a relatively low pyroclast mass emission (280 kg per event on average) and a

relatively low number of detected particles (180 per event on average) was measured (Figs. 4b and 4d). On average, the mean particle size was 6 cm (with a maximum value of 46 cm) and the vent-leaving velocity was 50 m/s (with a minimum and maximum values of 8 and 140 m/s, respectively).

Instead, ten type 1 explosions were fully recorded during the second period on 29 July. The minimum of pyroclast mass recorded for one of these events was 434 kg distributed between 1409 particles. In Figure 5c we give the FLIR image sequence for the explosion with the highest pyroclast mass emission recorded (2590 kg distributed between 5348 detected particles). Instead, in Figure 5d we give the FLIR image sequence of the explosion with the maximum number of detected particles (9029, representing a total of 880 kg). For all recorded type 1 explosions in the second period, a relatively high pyroclast mass emission (2400 kg per event on average, one order of magnitude higher than the type 0 explosions) and relatively high number of detected particles (5260 per event on average, also one order of magnitude higher than the type 0 explosions) were measured (Figs. 4b and 4d). On average, the mean particle size was the same as in the first period (6 cm; with a maximum measured value of 46 cm), but the vent-leaving velocity was lower (30 m/s, with a minimum and maximum values of 6 and 187 m/s respectively). All parameters extracted from the FLIR camera data are available in Table S2.

3.3. Explosive SO_2 mass emission

During the entire survey period, two gas plume measurements associated with two different type 0 explosions within the SW crater, were exploitable; both collected on 27 July (Fig. 6). Other measurements were not good enough due to heavy condensation within the gas plumes or cloud formation. These two exploitable measurements yielded SO_2 masses (Fig. 4d) of 2.61 ± 0.67 kg (explosion measured at 14:54; all times are local) and 2.07 ± 0.50 kg (explosion measured at 15:21). Values, assumptions and conversions applied to obtain these masses are given in Table S3.

3.4. Persistent SO_2 flux

The persistent SO_2 flux (Figs. 4c and 4d) also clearly discriminates the two periods. During the first period, the 121 Scanning DOAS measurements emphasize a persistently high SO_2 flux that fluctuated between 73 ± 11 t/d (= 0.84 kg/s) and 693 ± 6 t/d (= 8.02 kg/s) with a mean value of 274 t/d (= 3.17 kg/s). The second period, that includes 130 Scanning DOAS profiles, highlights a drop in the SO_2 flux. This is more than three time less than in the first period, with an average of 82 t/d (= 0.95 kg/s), the minimum flux being 26 ± 14 t/d (= 0.30 kg/s) and the maximum being 206 ± 4 t/d (= 2.38 kg/s). All values and errors are given in Table S4.

3.5. Ash fallout characteristics

Two ash samples were collected from two distinct type 0 explosions on the 25 and 27 July, and an ash sample representative of six type 1 explosions was collected on 29 July (Fig. 4d). Ash fallouts were systematically experienced around 2 minutes after the explosions occurred. Syn-eruptive GSDs directly measured by the ASHER were comparable with laboratory sieving data with a similar grain size range of between 63 and 710 µm for all samples (Fig. 7). No specific GSD differences appear between the type 0 and type 1 ash particles, with GSD modes ranging between the 180-250 µm and 355-500 µm bins for laboratory sieving (wt%) and between the 125-180 and 180-250 µm bins for ASHER syn-eruptive data (Fig. 7).

Componentry analysis performed on the three ash samples (Figs. S1, S2 and S3), and on the 180-250 µm grain size bin, identifies four different types of particles within the bulk samples (Fig. 8a), which are described hereafter in order of abundance. The first are sideromelane particles that are characterized by glassy matrixes with the presence of rounded vesicles and very scarce microlites. These particles either show fluidal, spongy or dense textures. They appear transparent to light brown under the binocular microscope.

The second are tachylite particles that are characterized by fully microcrystalline matrixes with the presence of very scarce irregular-shaped vesicles. They appear dark and opaque under the binocular microscope. Thirdly, phenocryst-free particles are observed (olivine, pyroxene and plagioclase in order of decreasing abundance) and counted as such as soon as the phenocryst represents more than 50 % of the entire particle. Finally, scarce altered particles are observed. These are characterized by highly altered features. They often appear red under the binocular microscope. The componentry analysis shows similar results between the two type 0 samples. However, slight differences are observed between the ash collected between the type 0 and type 1 explosions. Sideromelane particles are less abundant in the type 0 (49 % on average) than in the type 1 (64 %) samples. Tachylite particles are also more abundant in the type 0 samples (18 % on average) than in the type 1 sample (8 %). Similar proportions of phenocryst-free and altered particles are found between the two sample types (Fig. 8a). APASH measurements reveal only very subtle differences between the type 0 and type 1 ash samples (Fig. 8b) which can be attributed to the slight differences in the component proportions between the corresponding samples. In the type 1 ash sample, another particle population (highlighted by the red circle in Fig. 8b) appears, which is mainly characterized by the occurrence of particles with a higher morphological roughness range, mainly composed of sideromelane particles. In-situ glass chemical analysis performed on the sideromelane particles (Fig. 8c) show that the emitted magmas, both during type 0 and type 1 explosions, are part of the Highly Porphyritic (HP) composition field, which is typical of the normal Stromboli activity. Only scarce glass fragments fall in the stagnant magma composition field as defined by Gurioli et al. (2014). No significant chemical differences are observed between the two types of explosions. Raw data on the ash particle characterization is available in Table S5.

4 Discussion

4.1. Link between the pyroclast mass and persistent degassing

Our vent-leaving pyroclast emission parameters recorded during 13 different Strombolian explosions within the SW crater (Figs. 4b and 4d; Table S2) are consistent with those already recorded during normal explosive activity at Stromboli which show a typical range of 10 to 10^3 kg (e.g. Chouet et al. 1974; Blackburn et al. 1976; Weill et al. 1992; Ripepe et al. 1993; Hort and Seyfried 1998; Patrick et al. 2007; Taddeucci et al; 2012; Harris et al. 2013; Bombrun et al. 2015; Leduc et al. 2015; Gaudin et al. 2017; Pioli and Harris 2019). Our measurements confirm that gas-dominated type 0 explosions (Figs. 5a and 5b) produce relatively low total pyroclast masses (between 5 and 645 kg for a single event) with low numbers of particles (between 11 and 456 for a single event). Instead, type 1 explosions (Figs. 5c and 5d) produce relatively high total pyroclast masses (between 434 and 2589 kg for a single event) and involve higher numbers of particles (between 1409 and 9029 for a single event).

Our two explosive SO_2 mass measurements show relatively low values (between 2 and 3 kg per event; Fig. 4d; Table S3), which fall within the lowest range of previous measurements made at Stromboli (e.g. Mori and Burton 2009; Tamburello et al. 2012; Barnie et al. 2015). Likewise our 251 persistent SO_2 measurements of between 26 and 693 t/d; Figs. 4c and 4d; Table S4) overlap with other studies, where Allard et al. (1994) found persistent SO_2 degassing fluxes between 340 and 1420 t/d. This highlights that persistent degassing represents a variable, but much higher flux, than the explosive SO_2 flux. If we take a typical event frequency of five explosions per hour we obtain a total explosive flux of just 0.3 t/d. This is in agreement with Mori and Burton (2008) who found that the explosive SO_2 flux at Stromboli represents a relatively small contribution (3 to 8 %) of the total degassing budget compared to persistent flux (92 to 97%). Likewise, Tamburello et al. (2012) showed that puffing, which is generally located within the Central crater, emits twice as much gas as

Strombolian explosions. Thus, although Stromboli's explosions make for a spectacular distraction, the system is really dominated by persistent degassing.

Previous studies at Stromboli, especially before or during uncommon eruptive activity (i.e. paroxysmal or effusive, see terminology in Rosi et al. 2013), already showed that explosive degassing and persistent degassing fluxes are correlated (Delle Donne et al. 2017), which are also correlated with the explosion amplitudes (Ripepe et al. 2007; 2009; Valade et al. 2016). Thus, these parameters have become critical monitoring and potential precursors to uncommon and potentially dangerous eruptive activity. This is in contrast to the case documented here for normal, very mild, activity: our specific multi-parametric field experiment, performed on the short period of 25-30 July 2016 highlights that the explosive dynamics (explosion type, particle mass and number) observed on the main active vent within the SW crater are not at-all coupled with the total persistent SO_2 degassing flux (Fig. 4). This de-coupling is indeed revealed by the two distinct periods of degassing and activity style. During the first period, the persistent SO_2 degassing flux was relatively high (274 t/d on average, with peaks near 700 t/d), but activity was dominated by type 0 explosions and emitted particle masses were low. During the second period, the persistent SO_2 degassing flux declined by more than three times (to 82 t/d on average, with lowest values near 25 t/d) compared to the first period, and mainly type 1 explosions occurred (without any type 0 explosions) and the mass and number of tephra particles increased by two and three orders of magnitude, respectively. To sum up, we observe a strong anti-correlation between the amount of magma being degassed and the mass of pyroclasts being ejected from the main active vent (SW crater), as already documented by Leduc et al. (2015). We note, though, that during our observation period, the NE crater was not at all active, where we witnessed just seven exceedingly weak type 2 eruptions emitting ash to no more than a few tens of meters above the crater rim during the observation period. The Central crater, though, was active with its characteristic puffing behavior (e.g. Harris and Ripepe 2007a; Ripepe et al. 2007; Tamburello et al. 2012), emitting around one gas puff every two seconds, but not being the source of significant normal explosive activity with only two events observed during the whole observation period; the primary source of explosive activity being our targeted vent: the SWC.

4.2. Insights from ASHER measurements and ash characterization

During this experiment, the ASHER was installed for the first time in an active fall out field. It was thus important to check and validate its operation. The number of counted ash particles by the ASHER (384, 33 and 381 for the STR160725_1, STR160727_7 and STR160728_12 samples, respectively) differ from the actual number of particles counted in the bulk sample (830, 650 and 7974 respectively). This is due to the sampling interval of the instrument. ASHER GSDs are slightly skewed toward finer grain size bins compared the laboratory sieving analyses (Fig. 7). This is explained by the fact that ASHER GSD histograms represent the number of detected particles while laboratory sieving ones represent the total weight of the each grain size bins (the finer the particle, the lighter they are). We thus argue that GSDs acquired with these two different methods show coherent results. Moreover, no significant GSD differences are observed between the type 0 and type 1 explosions, both looking at the vent-leaving particles (FLIR measurements) and the ash fallout from the associated drifting cloud (ASHER and laboratory measurements). At vent, lapilli and bombs (up to 46 cm in width) are observed with a mean particle size of 7 and 6 cm for type 0 and type 1 explosions respectively. For the sampled ash particles, GSDs systematically comprise a range between 63 and 710 µm, which represent the size range of the coarsest particles carried by the drifting cloud, the finest particles being transported further. Terminal velocity values measured by the ASHER were between 0.1-0.5 and 1-2 m/s depending the grain size bins, and are coherent with those recorded by Fréret-Lorgeril et al. (2019).

The different ash components (Fig. 8a) identified in our samples were consistent with previous observations made for samples collected during normal activity at Stromboli (e.g. D'Oriano et al. 2010; Lautze et al. 2012; 2013). Textures of sideromelane particles are typically formed by HP magmas during normal Strombolian activity. No highly vesicular particles are observed, which suggest the absence of Low Porphyritic (LP) magmas. The dominant contribution of HP magmas to ash formation, with scarce stagnant superficial magma, is confirmed by the in situ glass analyses (Fig. 8c). The scarcity of a stagnant magma, microlite-rich component in the ash particles, is explained by the fact that the stagnant magma is not efficiently fragmented, only forming coarse pyroclasts that are mostly found in the vent-proximal zone (Gurioli et al. 2014; Leduc et al. 2015) and it only represents the "crust" at the top of the degassed magma, so volumetrically limited (as explained in Caracciolo et al. 2021). Tachylite particles are considered as fully crystallized stagnant magma or non-juvenile recycled particles. Phenocryst-free particles come from both juvenile and non-juvenile fraction. Altered particles are considered as non-juvenile lithic particles. A subtle but important ash component variation is observed: the proportion of juvenile (sideromelane) particles is greater for the type 1 explosion sample (64 %) than the type 0 explosion samples (49 %) looking at the 180-250 µm grain size bin. This difference is also identifiable in the APASH signature of the ash particles (occurrence of sideromelane, juvenile particles visible within the red circle in Fig. 8b). To sum up, no LP magma has been identified in the type 0 and type 1 products. The only significant difference between the ash samples from both explosion types is that juvenile particles are more present within the type 1 products than the type 0 ones. This observation suggests that type 1 explosions fragment a large proportion of degassed HP magma than type 0, in agreement with magma accumulation. In contrast, Type 0 emits less magma, but a larger proportion of non-juvenile particle than type 1 explosions because of free from magma accumulation and therefore prone at cleaning the conduit (e.g. Gurioli et al. 2014; Leduc et al. 2015; Gaudin et al. 2017).

4.3. An accidental driver for eruption magnitude: Implications for eruptive processes

The frequencies of the Strombolian explosions were the same in both observation periods. This indicates that for the whole investigated time, the magnitude, intensity, frequency and style of the explosive activity was not driven by, or linked to, deep processes that feed the persistent degassing flux that is changing from a period to another. Thus, measurements of the plume properties cannot be systematically used to assess or infer how active, in terms of persistent degassing, the system is. In fact, the reverse holds for the normal mild activity (without coupling between gas and particles): the more abundant is the material emitted, the less intense the degassing activity is (Fig. 4). This confirms that the magma erupted at such systems is, at least for some periods during normal Strombolian activity, in no way associated with the magma that is degassed to drive the persistent SO_2 flux at such systems. This is consistent with the idea that processes controlling fragmentation at Stromboli can be driven from relatively superficial parameters, where the explosivity is controlled by the presence, and thickness, of a thin and viscous cap on the magma column (e.g. Burton et al. 2007a; Gurioli et al. 2014; Barnie et al. 2015; Leduc et al. 2015; Gaudin et al. 2017; Simons et al. 2020). From these previous models, we can argue that type 0 explosions are characterized by a low content of particles because they occurred when the shallow part of the eruptive conduit contains no (or little) degassed magma. Instead, the presence of degassed magma adds particles, but poor fragmentation efficiency in the high viscosity caps result in bomb-dominated type 1 explosions. The presence of any recycled backfill material will then be enhancing type 2 explosions (e.g. Patrick et al. 2007; Capponi et al. 2016; Simons et al. 2020). Our data support this global model for type 0 and 1 explosions whereby the mass of the bomb load accompanying an explosive event depends on the volume of the degassed magma cap sitting at the head of the magma column. The thicker the degassed magma cap, the greater quantity of material is available for the slug to fragment so that the emission carries a greater accidental bomb and lapilli load. Lower vent-leaving

particle velocities (33 m/s on average) for type 1 explosions compared to the type 0 velocities (46 m/s on average) are also consistent with the model presented in Gaudin et al. (2017).

According to our data, the association of type 1 explosions with relatively low persistent gas flux periods suggests that periods of reduced degassing allow caps to build, while relatively high persistent gas flux periods do not allow cap formation. Our model is also consistent with the observed spatial pattern of activity. That is, the Central crater is believed to be the main, central pathway for gas ascent, hosting the hottest magma (Harris and Ripepe 2007b; Landi et al. 2011) and being the source of around 70 % of the active degassing, that is represented by the gas released by the explosions and puffing (Tamburello et al. 2012). The lack of normal activity at this location would thus be explained by lack of cap formation at this focused source of degassing. As in other studies, the switch between low and high degassing periods occurs as a step, the change happening at most over an hour or two (e.g. Ripepe et al. 2002; 2008). Here, we also see that the cap responds over a similar time scale, but may be slightly lagged as the cap become reamed out at the onset of high degassing phase: eruptions continue at the same frequency, but steadily exhaust the superficial reservoir of stagnant cap magma.

As shown by Burton et al. (2007a; 2007b), gas slug formation and persistent degassing likely has its origin in relatively deep levels between sea level and near the volcano/crust interface (around 2 km below sea level, and 3 km below the summit craters). Moreover, Burton et al. (2007a; 2007b) showed that the depth of slug formation may highly modulate the explosion intensities at the surface, the smallest explosions being produced by relatively small shallow slugs and the largest explosions being produced by large deep slugs. We thus support that while the mass of gas in an explosive normal event is controlled by deep processes, the mass of pyroclasts is rather controlled by shallow processes so that the two masses do not, necessarily, correlate. We suggest that these deep magmatic processes, especially persistent degassing fluctuations, can rapidly influence the superficial structure of the eruptive conduit, modulating the presence or the absence of degassed magma at the explosion/fragmentation level. When deep-seated magma-gas-coupled, enter the system, then the correlation between explosivity and mass flux and gas flux is reestablished.

5 Conclusion

In this study, we present a multi-parametric monitoring methodology, based on ground-based remote sensing, for tracking activity at persistently degassing Strombolian systems, and present a framework within which to assess coupled variations in tracked parameters. Our combined measurements, on a short and specific period during normal Strombolian activity at Stromboli, highlight that low levels of degassing can be associated with establishment of a degassed magma cap at the conduit head, which contributes to the bomb load for type 1 eruptions. Instead, high levels of persistent degassing can be associated with the occurrence of gas-dominated type 0 gas jets, with very few particles.

Essentially, if there were no degassed cap, Strombolian eruptions at Stromboli would not be characterized by the bomb emission with which they have so famously become associated (e.g. Mercalli 1906; Macdonald 1972; Francis 1993). Instead, pure normal Strombolian activity in a system which is purely driven from the deeper source would be mainly characterized by gas jetting. However, the top down influence exerted by the presence of a cap or scoria vent-choking material means that bombs and ash are invariably involved, with greater bomb loads implying an increasing influence of the cap and greater ash loads indicating a greater role of scoria choking (e.g. Cappioni et al. 2016; Simons et al. 2020). We suggest that relatively low persistent degassing fluxes allow preservation, formation and accumulation of viscous caps within the shallow eruptive conduits near the fragmentation level. Instead, relatively high degassing rates promote cap-free conditions, so that gas bursts typically provoke type 0 explosions. Drops in persistent degassing flux thus rapidly favor

the formation of a degassed magma cap, enhancing the occurrence of type 1 explosions. Type 2 explosions are probably more independent with this process as this explosion type is more likely provoked by relatively thick and dense cap formed by recycled backfill material.

In parallel to our results and associated model, it is important to keep in mind that monitoring measurements also usually show that mass loads for normal Strombolian activity at the NE and SW craters increase during periods of enhanced tremor, degassing and puffing, allowing prediction of the arrival of uncommon and larger explosive or effusive activity at Stromboli (e.g. Ripepe et al. 2007; 2009; Valade et al. 2016; Delle Donne et al. 2017). This suggests that the system switchs between a decoupling magma-gas behavior versus a coupled magma-gas system due to the arrival of deep-seated gas-rich magma and that the cap formation may be variable from crater to crater, and can persist at some craters/vents during increases in gas flux, especially if the central crater takes the main burden. We conclude that solid masses erupted during normal/mild Strombolian activity could inform little on the actual state of the system, but instead could be a measure of the quantity of degassed material sitting at the head of the eruptive conduit. Indeed, the gas can be completely decoupled from the magma it fragments: the gas having been sourced from several kilometers of depth, but the fragments being sourced from just a few tens of meters of depth (Harris et al. 2013). Therefore, persistent degassing flux is a better parameter to track deeper magmatic processes that determine the volumes of gas involved in explosive events. The link documented here between persistent degassing and eruptive dynamics can provide indirect information of the real magmatic state of the volcano: emissions characterized by bomb-poor gas jetting are indicative of a highly charged system in gas. Instead, systems with high and sustained bomb masses likely imply the presence, and persistence, of a cap (e.g. Leduc et al. 2015; Gaudin et al. 2017; Simons et al. 2020).

6 Figures

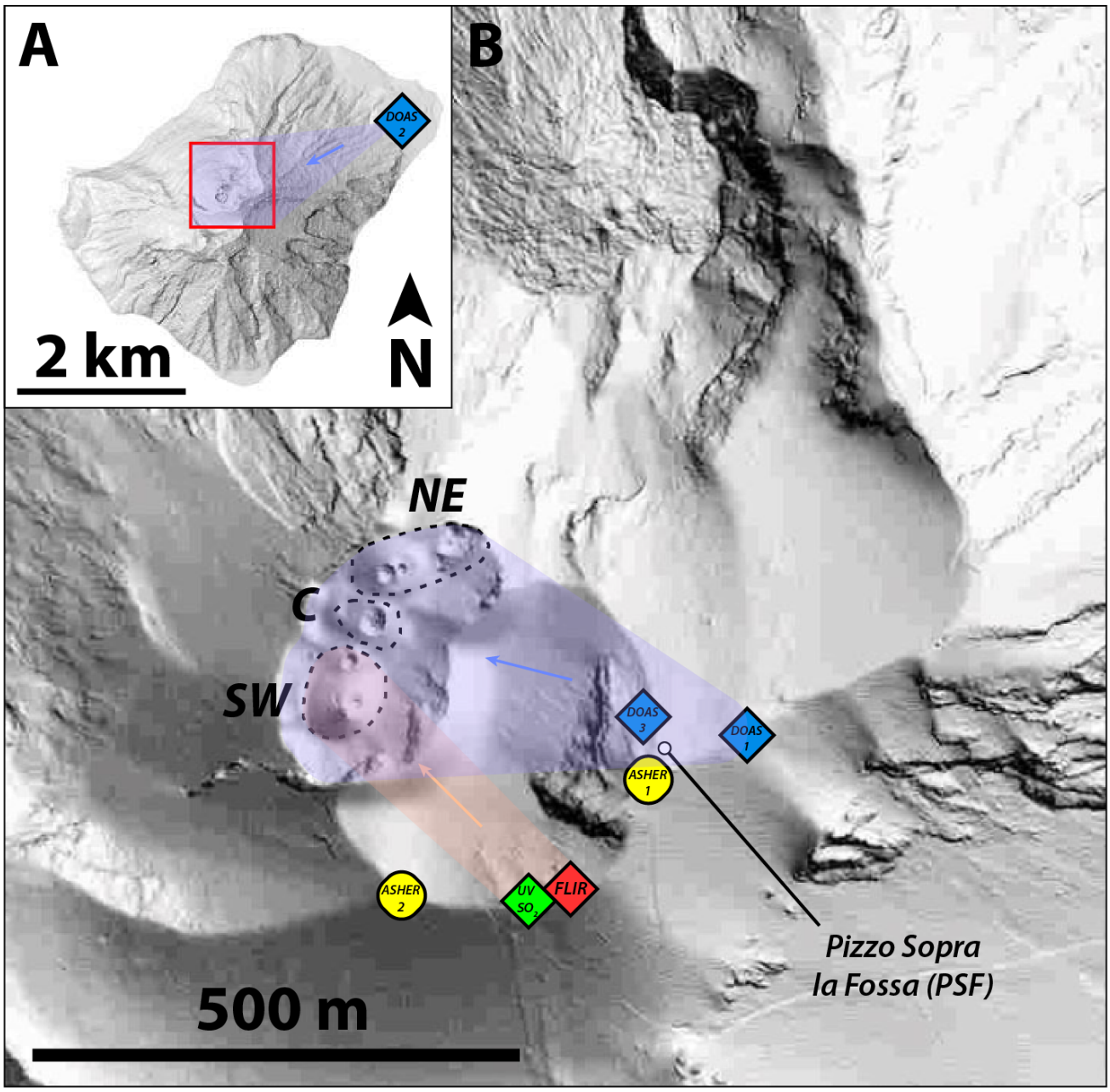


Figure 1 – (a) Digital Elevation Model (DEM) of Stromboli Island, with the location of the Differential Optical Absorption Spectroscopy (DOAS) instrument. (b) DEM of the summit area of Stromboli volcano with the locations of the Forward Looking Infra-Red (FLIR) camera, the Ultra-Violet (UV) SO_2 camera, the ASH collector and sizER (ASHER) instrument (2 different positions), and the DOAS instrument (2 different positions). The three different active zones of Stromboli volcano are materialized: the South-West (SW) crater, the Central (C) crater, and the North-East (NE) crater.

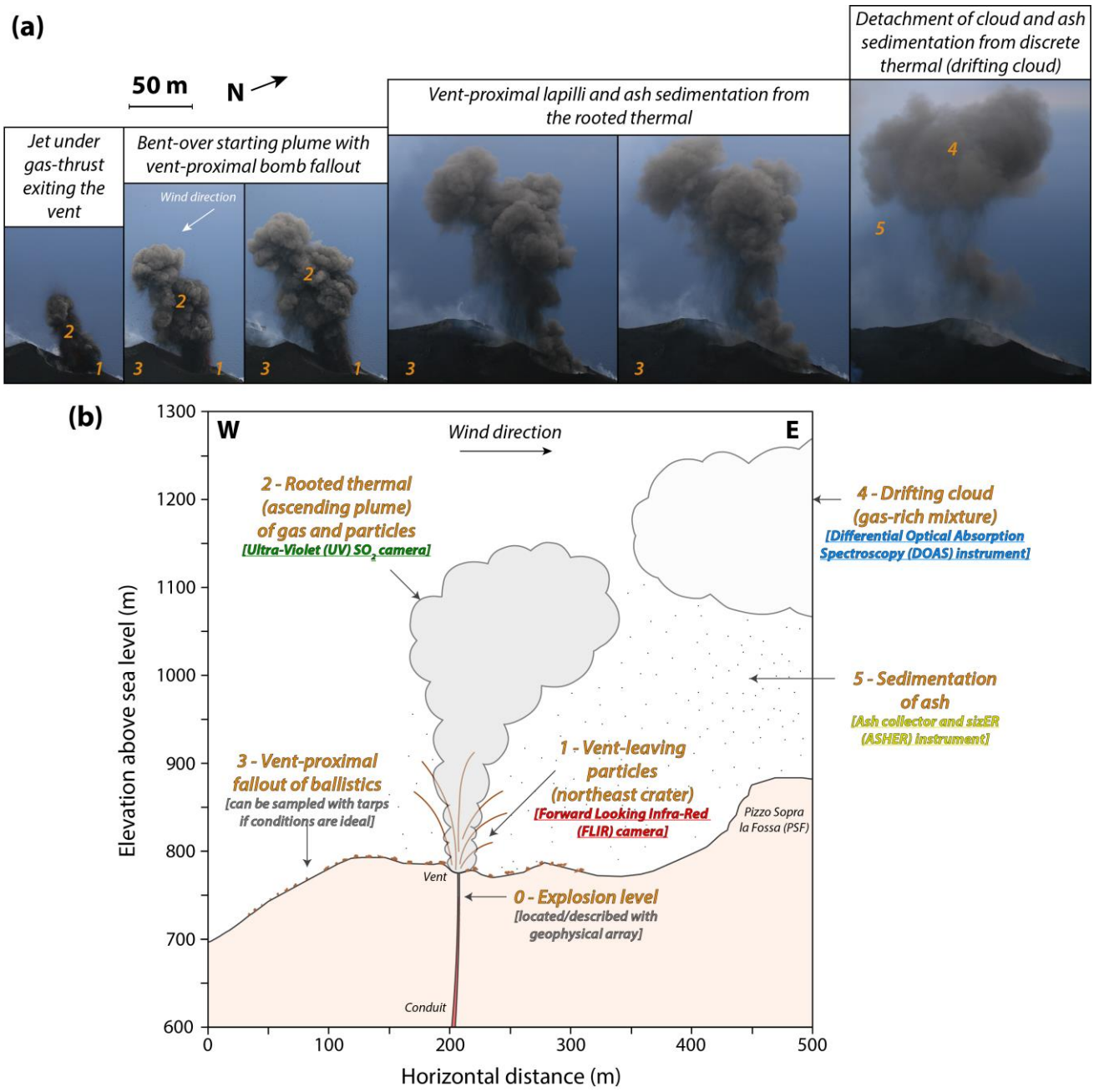


Figure 2 – (a) Sequence of pictures of a Type 2a explosion at Stromboli volcano, representing the evolution of eruptive products (ballistics and plume) in the atmosphere since the explosion level. Orange numbers are described in (b). Terminology is based on Turner (1962; 1969) and Slawson and Csanady (1967). (b) Sketch of the different steps (marked in orange) of a normal explosion at Stromboli. Each steps can be sampled and/or measured by different techniques and/or strategies, which are listed in text. Instruments used in our field experiments are underlined in different colors following the one used in Figure 1.



Figure 3 – (a) FLIR camera aiming pyroclasts from the South West (SW) crater. (b) Ultra-Violet (UV) SO_2 camera aiming volcanic plumes from the SW crater. (c) ASH collector and sizER (ASHER) instrument measuring and collecting ash fallouts. In the background, panorama of the Central (on the left) and the North East (on the right) active craters of Stromboli volcano in July 2016. (d) Differential Optical Absorption Spectroscopy (DOAS) instrument with the summit area of Stromboli in the background.

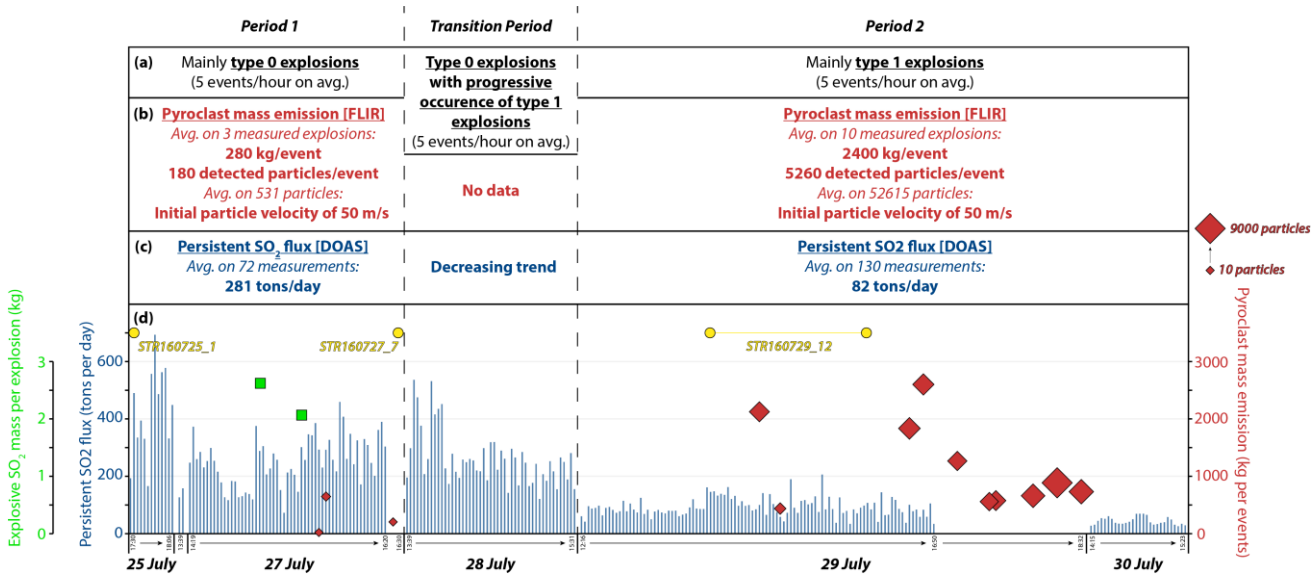


Figure 4 – Field experiment results performed between 25 July 2016 and 30 July 2016. (a) Field observations. (b) Summary of the pyroclast mass emissions measured with the Forward Looking Infra-Red (FLIR) camera. (c) Summary of the persistent SO_2 fluxes measured with the Differential Optical Absorption Spectroscopy (DOAS) instrument. (d) Detailed timeline of the performed measurements. Red squares represent the pyroclast mass emissions during type 0 and 1 explosions, calculated from the FLIR acquisitions; the size of the red squares is proportional to the number of the detected particles. Green squares are the two explosive SO_2 measurements from the Ultra-Violet (UV) SO_2 camera. Yellow circles represent the explosions related to the three exploitable ash samples collected by the ASH collector and sizER (ASHER) instrument.

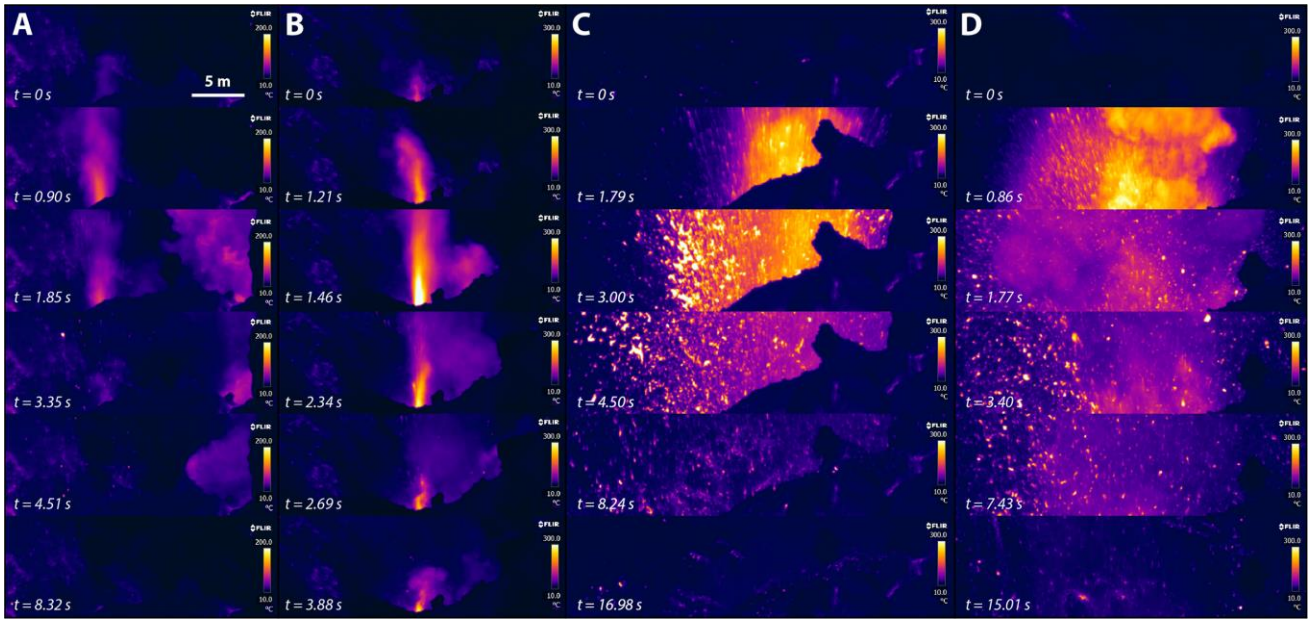


Figure 5 – Sequences of images of four explosions in the South West (SW) crater, recorded with the Forward Looking InfraRed (FLIR) camera. (a) Type 0 explosion recorded the 27 July at 13:43 (all times quoted in this paper are local times). At t = 0 s, only intermittent gas puffing is observed; between t = 0.90 s and t = 1.85 s, the explosion begins, a gas jet is visible with temperature up to 200 °C, with the synchronous emission of scarce particles; between t = 3.35 s and t = 4.51 s, the gas jet decreases, still with the emission of scarce particles; at t = 8.32 s, the explosion ends. (b) Type 0 explosion recorded the 27 July at 16:26. At t = 0 s, only intermittent gas puffing is observed; between t = 1.21 s and t = 1.46 s the explosion begins, a gas jet is visible with temperature more than 300 °C; between t = 2.34 s and t = 2.69 s, the gas jet decreases in intensity with the emission of very scarce particles; at t = 3.88 s, the gas jet ends. (c) Type 1 explosion recorded the 29 July at 14:44. At t = 0 s, no particles and no gas puffing are visible; at t = 1.79 s, the explosion starts with the emission of a lot of particles; at t = 3.00 s, the explosions intensity reach its maximum in term of pyroclast mass emission; between t = 4.50 s and t = 8.24 s the explosion decreases; at t = 16.98 s, the explosion ends with still hot pyroclasts on the crater walls. (d) Type 1/2 explosion recorded the 29 July at 16:16. At t = 0 s, no particles and no gas puffing are visible; at t = 0.86 s, the explosion starts with the emission of a lot of particles with a distinguishable small ash and/or gas plume; between t = 1.77 s and t = 7.43 s the explosion oscillates in term of intensity with the emission of a lot of relatively fine particles (lapilli); at t = 15.01 s, the explosion ends with still hot pyroclasts on the crater walls.

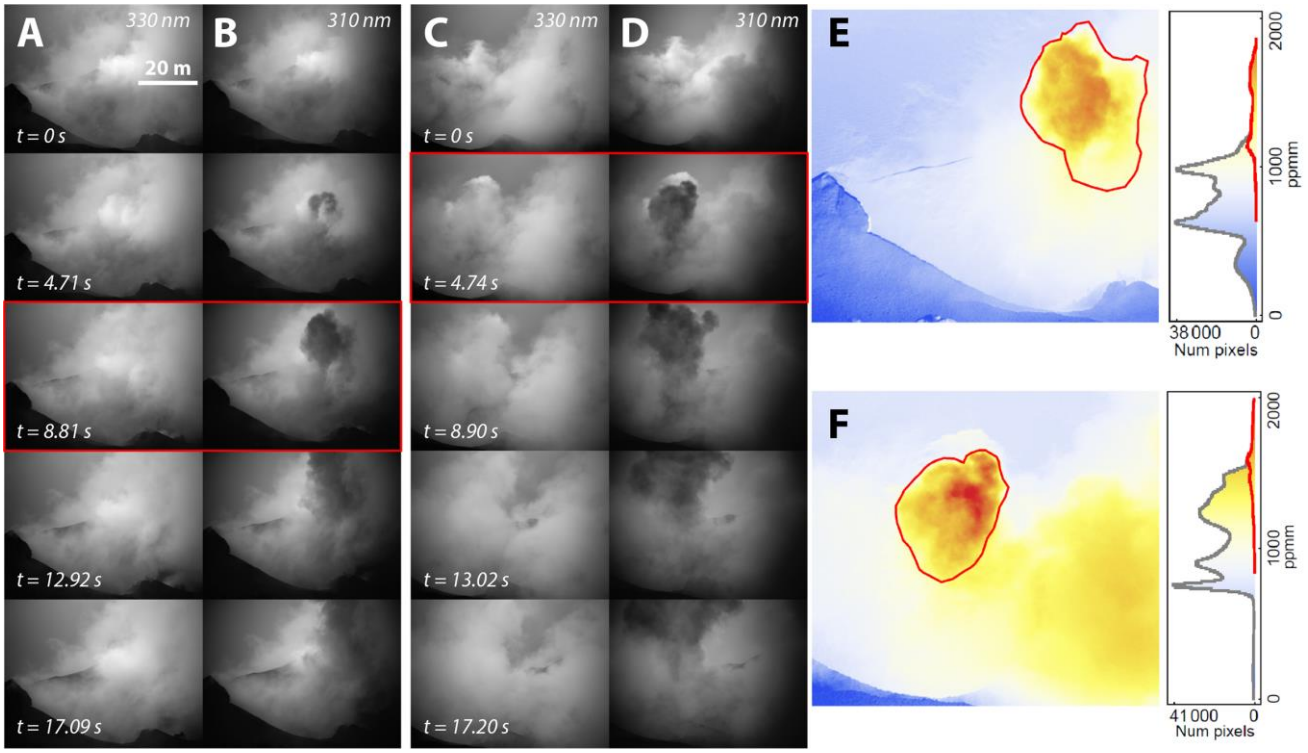


Figure 6 – Sequences of images of the two exploitable SO_2 plumes above the SW crater, 27 July, recorded with the Ultra-Violet (UV) SO_2 camera. (a) and (b) Plume recorded at 14:54. (c) and (d) Explosion recorded at 15:21. (a) and (c) are 330 nm images (no SO_2 absorption). (b) and (d) are 310 nm images (SO_2 absorption). The SO_2 plume is visible on the 310 nm images in black. Image pairs framed in red were chosen to calculate Apparent Absorption (AA) images and calibrated SO_2 images in ppmm that are represented in (e) and (f) for the 14:54 and 15:21 explosions respectively. Eruption plumes are outlined in red. Histograms to the right of both images show the image (grey curve) and plume (red curve) ppmm distributions.

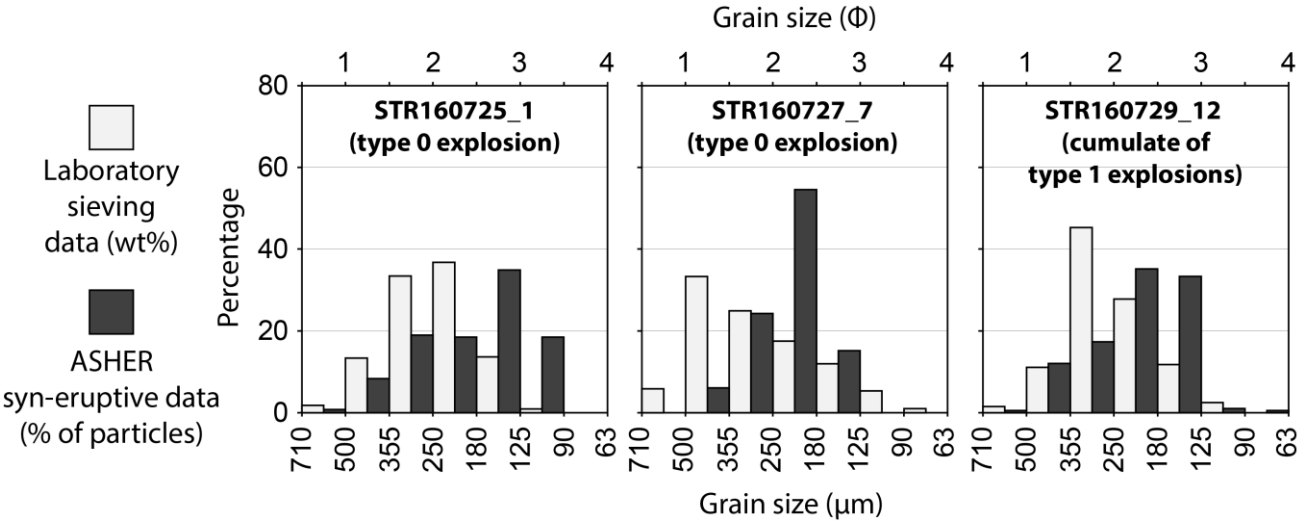
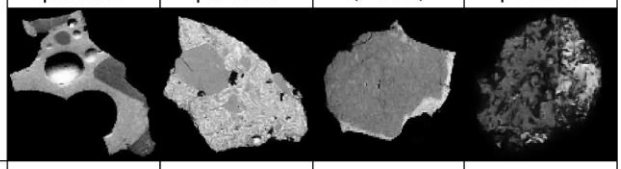


Figure 7 – Grain size of the three collected ash samples measured both by the ASH collector and sizER (ASHER) instrument and by laboratory sieving.

(a)

	Sideromelane particles	Tachylite particles	Phenocryst (> 50%)	Altered particles
SEM-BSE images				
STR160725_1 (type 0)	47% (319)	16% (109)	28% (191)	9% (60)
STR160727_7 (type 0)	51% (34)	21% (14)	24% (16)	4% (3)
STR160729_12 (type 1)	64% (351)	8% (42)	22% (123)	6% (32)

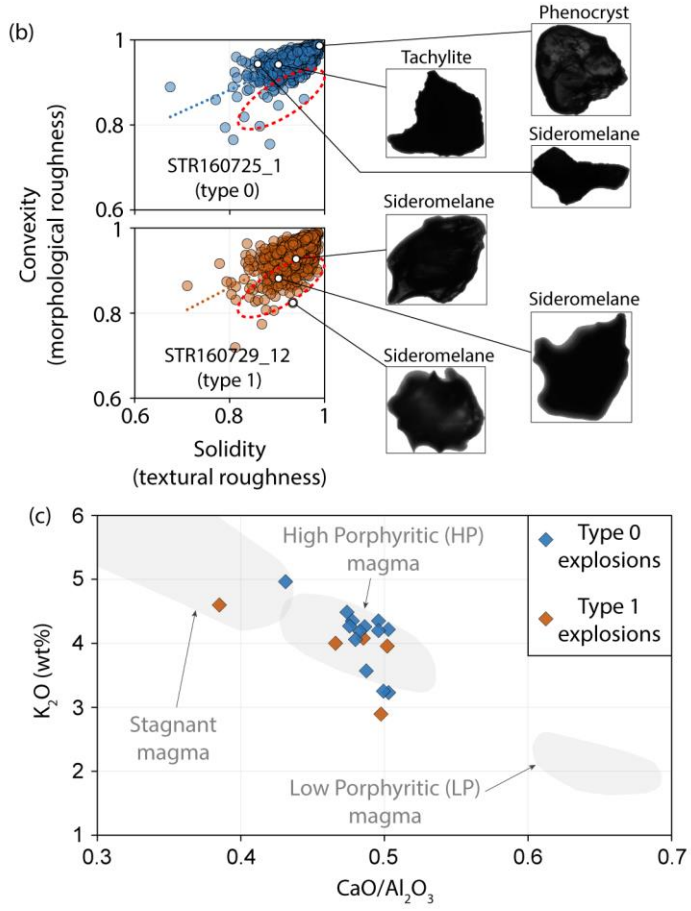


Figure 8 - (a) Componentry analysis of the three collected samples performed within the 180-250 µm grain size bin and using Back-Scattered Electron (BSE) images acquired with a Scanning Electronic Microscope (SEM). The percentage of each component is derived from the number of particles identified and counted manually (the numbers of counted particle are represented in parentheses). (b) Apparent Projected shape of ASH (APASH) for the STR160725_1 (type 0 explosion) and STR160729_12 (type 1 explosions) samples, represented within the Solidity vs. Convexity graphs. Linear trends are represented by the dashed lines. The red circle show the same area in both graphs, evidencing the occurrence of another ash population for the STR160729_12 sample. (c) In-situ glass compositions of the sideromelane particles. The different composition fields were reconstructed from Métrich et al. (2005), Gurioli et al. (2014), Pioli et al. (2014), Leduc et al. (2015) data.

7 Author Contributions

ST performed the ash analysis, participated to the discussion, wrote the manuscript and created the figures. AH, LG, PB, TB, MB and EM performed the field experiments, participated to the discussion and reviewed the manuscript.

8 Funding, acknowledgments and conflict of interest statement

We thank J-L. Devidal for its invaluable help with the EPMA at LMV. This is a contribution among some VOs and VRIs of WP4 and WP8 of EUROVOLC. This project has received funding from the European Union's Horizon 2020 research and innovation program under grant agreement N°731070 and this research was financed by the French government IDEX-ISITE initiative 16-IDEX-0001 (CAP 20-25). The ASHER machine was purchased by the ANR-STRAP project funded by the Agence Nationale de la Recherche (ANR-14-CE03-0004-04). This is Laboratory of Excellence ClerVolc contribution number 483.

9 Reference list

Aiuppa, A., Federico, C., Giudice, G., Giuffrida, G., Guida, R., Gurrieri, S., … Papale, P. (2009). The 2007 eruption of Stromboli volcano: Insights from real-time measurement of the volcanic gas plume CO2/SO2 ratio. Journal of Volcanology and Geothermal Research, 182(3-4), 221–230. doi:10.1016/j.jvolgeores.2008.09.013

Allard, P. (1997). Endogenous magma degassing and storage at Mount Etna. Geophysical Research Letters, 24(17), 2219–2222. doi:10.1029/97gl02101

Allard, P., Carbonnelle, J., Métrich, N., Loyer, H., & Zettwoog, P. (1994). Sulphur output and magma degassing budget of Stromboli volcano. Nature, 368(6469), 326–330. doi:10.1038/368326a0

Barberi, F. (1993). Volcanic hazard assessment at Stromboli based on review of historical data. Acta Vulcanologica, 3, 173-187

Barnie, T., Bombrun, M., Burton, M. R., Harris, A., and Sawyer, G. (2015). Quantification of gas and solid emissions during Strombolian explosions using simultaneous sulphur dioxide and infrared camera observations. Journal of Volcanology and Geothermal Research, 300, 167–174. doi:10.1016/j.jvolgeores.2014.10.003

Bertolaso, G., De Bernardinis, B., Bosi, V., Cardaci, C., Ciolli, S., Colozza, R., … Soddu, P. (2009). Civil protection preparedness and response to the 2007 eruptive crisis of Stromboli volcano, Italy. Journal of Volcanology and Geothermal Research, 182(3-4), 269–277. doi:10.1016/j.jvolgeores.2009.01.022

Blackburn, E.A., L. Wilson, and Sparks, R.S.J. (1976). Mechanisms and dynamics of strombolian activity. Journal of the Geological Society 132.4 (1976): 429-440. doi: 10.1144/gsjgs.132.4.0429

Bogumil, K., Orphal, J., Homann, T., Voigt, S., Spietz, P., Fleischmann, O. ., … Burrows, J. (2003). Measurements of molecular absorption spectra with the SCIAMACHY pre-flight model: instrument characterization and reference data for atmospheric remote-sensing in the 230–2380 nm region. Journal of Photochemistry and Photobiology A: Chemistry, 157(2-3), 167–184. doi:10.1016/s1010-6030(03)00062-5

Bombrun, M., Harris, A., Gurioli, L., Battaglia, J., & Barra, V. (2015). Anatomy of a Strombolian eruption: Inferences from particle data recorded with thermal video. Journal of Geophysical Research: Solid Earth, 120(4), 2367–2387. doi:10.1002/2014jb011556

Bombrun, M., Barra, V., and Harris, A. (2014). Algorithm for particle detection and parameterization in high-frame-rate thermal video. Journal of Applied Remote Sensing, 8(1), 083549. doi:10.1117/1.jrs.8.083549

Branan, Y. K., Harris, A., Watson, I. M., Phillips, J. C., Horton, K., Williams-Jones, G., & Garbeil, H. (2008). Investigation of at-vent dynamics and dilution using thermal infrared radiometers at Masaya volcano, Nicaragua. Journal of Volcanology and Geothermal Research, 169(1-2), 34–47. doi:10.1016/j.jvolgeores.2007.07.021

Braun, T., & Ripepe, M. (1993). Interaction of seismic and air waves recorded at Stromboli Volcano. Geophysical Research Letters, 20(1), 65–68. doi:10.1029/92gl02543

Burton, M. R., Sawyer, G. M. (2016): iFit: An intensity-based retrieval for SO2 and BrO from scattered sunlight ultraviolet volcanic plume absorption spectra, Atmos. Meas. Tech. Discuss., https://doi.org/10.5194/amt-2015-380

Burton, M. R., Caltabiano, T., Murè, F., Salerno, G., & Randazzo, D. (2009). SO2 flux from Stromboli during the 2007 eruption: Results from the FLAME network and traverse measurements. Journal of Volcanology and Geothermal Research, 182(3-4), 214–220. doi:10.1016/j.jvolgeores.2008.11.025

Burton, M., Allard, P., Mure, F., & La Spina, A. (2007a). Magmatic Gas Composition Reveals the Source Depth of Slug-Driven Strombolian Explosive Activity. Science, 317(5835), 227–230. doi:10.1126/science.1141900

Burton, M. R., Mader, H. M., & Polacci, M. (2007b). The role of gas percolation in quiescent degassing of persistently active basaltic volcanoes. Earth and Planetary Science Letters, 264(1-2), 46–60. doi:10.1016/j.epsl.2007.08.028

Businger, S., Huff, R., Pattantyus, A., Horton, K., Sutton, A. J., Elias, T., & Cherubini, T. (2015). Observing and forecasting vog dispersion from Kīlauea Volcano, Hawaii. Bulletin of the American Meteorological Society, 96(10), 1667-1686. doi:10.1175/BAMS-D-14-00150.1

Calvari, S., Spampinato, L., Lodato, L., Harris, A. J. L., Patrick, M. R., Dehn, J., … Andronico, D. (2005). Chronology and complex volcanic processes during the 2002-2003 flank eruption at Stromboli volcano (Italy) reconstructed from direct observations and surveys with a handheld thermal camera. Journal of Geophysical Research: Solid Earth, 110(B2). doi:10.1029/2004jb003129

Capponi, A., James, M.R., Lane, S.J. (2016). Gas slug ascent in a stratified magma: Implications of flow organisation and instability for Strombolian eruption dynamics. Earth Planet. Sci. Lett. 435, 159–170. doi:10.1016/j.epsl.2015.12.028

Caracciolo, A., Gurioli, L., Marianelli, P., Bernard, J., Harris, A.J.L. (2021). Textural and chemical features of a “soft” plug emitted during Strombolian explosions: A case study from Stromboli volcano. Earth and Planetary Science Letters, 559, 116761. doi.org/10.1016/j.epsl.2021.116761

Chouet, B., Dawson, P., Ohminato, T., Martini, M., Saccorotti, G., Giudicepietro, F., … Scarpa, R. (2003). Source mechanisms of explosions at Stromboli Volcano, Italy, determined from moment-tensor inversions of very-long-period data. Journal of Geophysical Research: Solid Earth, 108(B1), ESE 7–1–ESE 7–25. doi:10.1029/2002jb001919

Chouet, B., Saccorotti, G., Dawson, P., Martini, M., Scarpa, R., De Luca, G., … Cattaneo, M. (1999). Broadband measurements of the sources of explosions at Stromboli Volcano, Italy. Geophysical Research Letters, 26(13), 1937–1940. doi:10.1029/1999gl900400

Chouet, B., Hamisevicz, N., & McGetchin, T. R. (1974). Photoballistics of volcanic jet activity at Stromboli, Italy. Journal of Geophysical Research, 79(32), 4961–4976. doi:10.1029/jb079i032p04961

D'Oriano, C., Bertagnini, A., & Pompilio, M. (2010). Ash erupted during normal activity at Stromboli (Aeolian Islands, Italy) raises questions on how the feeding system works. Bulletin of Volcanology, 73(5), 471–477. doi:10.1007/s00445-010-0425-0

De Castro, E., Morandi, C., 1987. Registration of translated and rotated images using finite Fourier transforms. Pattern. Anal. Mach. Intell. IEEE Trans. PAMI-9 (5), 700–703.

Del Bello, E., Lane, S.J., James, M.R., Llewellin, E.W., Taddeucci, J., Scarlato, P., Capponi, A. (2015). Viscous plugging can enhance and modulate explosivity of strombolian eruptions. Earth Planet. Sci. Lett. 423, 210–218. doi:10.1016/j.epsl.2015.04.034

Delle Donne, D., Tamburello, G., Aiuppa, A., Bitetto, M., Lacanna, G., D'Aleo, R., & Ripepe, M. (2017). Exploring the explosive-effusive transition using permanent ultraviolet cameras. Journal of Geophysical Research: Solid Earth, 122(6), 4377–4394. doi:10.1002/2017jb014027

Francis, P., Oppenheimer, C., & Stevenson, D. (1993). Endogenous growth of persistently active volcanoes. Nature, 366(6455), 554–557. doi:10.1038/366554a0

Freret-Lorgeril, V., Donnadieu, F., Eychenne, J., Soriaux, C., Latchimy, T. (2019). In situ terminal settling velocity measurements at Stromboli volcano: Input from physical characterization of ash. Journal of Volcanology and Geothermal Research, 374, 62-79. doi:10.1016/j.jvolgeores.2019.02.005

Gaudin, D., Taddeucci, J., Scarlato, P., del Bello, E., Ricci, T., Orr, T., … Bucci, A. (2017). Integrating puffing and explosions in a general scheme for Strombolian-style activity. Journal of Geophysical Research: Solid Earth. doi:10.1002/2016jb013707

Gerst, A., Hort, M., Aster, R. C., Johnson, J. B., & Kyle, P. R. (2013). The first second of volcanic eruptions from the Erebus volcano lava lake, Antarctica-Energies, pressures, seismology, and infrasound. Journal of Geophysical Research: Solid Earth, 118(7), 3318–3340. doi:10.1002/jgrb.50234

Gresta, S., Ripepe, M., Marchetti, E., D'Amico, S., Coltelli, M., Harris, A. J. L., & Privitera, E. (2004). Seismoacoustic measurements during the July–August 2001 eruption of Mt. Etna volcano, Italy. Journal of Volcanology and Geothermal Research, 137(1-3), 219–230. doi:10.1016/j.jvolgeores.2004.05.017

Goto, A., Ripepe, M., & Lacanna, G. (2014). Wideband acoustic records of explosive volcanic eruptions at Stromboli: New insights on the explosive process and the acoustic source. Geophysical Research Letters, 41(11), 3851–3857. doi:10.1002/2014gl060143

Gurioli, L., Andronico, D., Bachelery, P., Balcone-Boissard, H., Battaglia, J., Boudon, G., … Thordarson, T. (2015). MeMoVolc consensual document: a review of cross-disciplinary approaches to characterizing small explosive magmatic eruptions. Bulletin of Volcanology, 77(6). doi:10.1007/s00445-015-0935-x

Gurioli, L., L. Colo', A. J. Bollasina, A. J. L.Harris, A. Whittington, and M. Ripepe (2014), Dynamics of Strombolian explo-sions: Inferences from field and labora-tory studies of erupted bombs fromStromboli volcano, J. Geophys. Res. SolidEarth, 119, 319–345, doi:10.1002/2013JB010355.

Gurioli, L., Harris, A. J. L., Colò, L., Bernard, J., Favalli, M., Ripepe, M., & Andronico, D. (2013). Classification, landing distribution, and associated flight parameters for a bomb field emplaced during a single major explosion at Stromboli, Italy. Geology, 41(5), 559–562. doi:10.1130/g33967.1

Gurioli, L., Harris, A. J. L., Houghton, B. F., Polacci, M., & Ripepe, M. (2008). Textural and geophysical characterization of explosive basaltic activity at Villarrica volcano. Journal of Geophysical Research: Solid Earth, 113(B8). doi:10.1029/2007jb005328

Harris, A. J. L., Delle Donne, D., Dehn, J., Ripepe, M., & Worden, A. K. (2013). Volcanic plume and bomb field masses from thermal infrared camera imagery. Earth and Planetary Science Letters, 365, 77–85. doi:10.1016/j.epsl.2013.01.004

Harris, A. J. L., Ripepe, M., & Hughes, E. A. (2012). Detailed analysis of particle launch velocities, size distributions and gas densities during normal explosions at Stromboli. Journal of Volcanology and Geothermal Research, 231-232, 109–131. doi:10.1016/j.jvolgeores.2012.02.012

Harris, A., & Ripepe, M. (2007a). Synergy of multiple geophysical approaches to unravel explosive eruption conduit and source dynamics – A case study from Stromboli. Chemie Der Erde - Geochemistry, 67(1), 1–35. doi:10.1016/j.chemer.2007.01.003

Harris, A., & Ripepe, M. (2007b). Temperature and dynamics of degassing at Stromboli. Journal of Geophysical Research, 112(B3). doi:10.1029/2006jb004393

Harris, A. J. L., & Stevenson, D. S. (1997). Magma budgets and steady-state activity of Vulcano and Stromboli. Geophysical Research Letters, 24(9), 1043–1046. doi:10.1029/97gl00861

Hort, M., & Seyfried, R. (1998). Volcanic eruption velocities measured with a micro radar. Geophysical Research Letters, 25(1), 113–116. doi:10.1029/97gl03482

Houghton, B.F., Taddeucci, J., Andronico, D., Gonnermann, H.M., Pistolesi, M., Patrick, M.R., Orr, T.R., Swanson, D.A., Edmonds, M., Gaudin, D., Carey, R.J., Scarlato, P. (2016). Stronger or longer: Discriminating between Hawaiian and Strombolian eruption styles. Geology 44, 163–166. doi:10.1130/G37423.1

Jaupart, C., & Vergniolle, S. (1989). The generation and collapse of a foam layer at the roof of a basaltic magma chamber. Journal of Fluid Mechanics, 203, 347. doi:10.1017/s0022112089001497

Jaupart, C., & Vergniolle, S. (1988). Laboratory models of Hawaiian and Strombolian eruptions . Nature, 331(6151), 58–60. doi:10.1038/331058a0

Johnson, J., Aster, R., Jones, K. R., Kyle, P., & McIntosh, B. (2008). Acoustic source characterization of impulsive Strombolian eruptions from the Mount Erebus lava lake. Journal of Volcanology and Geothermal Research, 177(3), 673–686. doi:10.1016/j.jvolgeores.2008.06.028

Kuglin, C.D., and Hines, D.C., (1975). The phase correlation image alignment method. Proceedings of the 1975 International Conference on Cybernetics and Society: 163–165.

Landi, P., Marchetti, E., La Felice, S., Ripepe, M., Rosi, M. (2011). Integrated petrochemical and geophysical data reveals thermal distribution of the feeding conduits at Stromboli volcano, Italy, Geophys. Res. Lett., 38, L08305. doi:10.1029/2010GL046296.

Lautze, N., Taddeucci, J., Andronico, D., Houghton, B., Niemeijer, A., & Scarlato, P. (2013). Insights into explosion dynamics and the production of ash at Stromboli from samples collected in real-time, October 2009. Geological Society of America Special Papers, 125–139. doi:10.1130/2013.2498(08)

Lautze, N. C., Taddeucci, J., Andronico, D., Cannata, C., Tornetta, L., Scarlato, P., … Lo Castro, M. D. (2012). SEM-based methods for the analysis of basaltic ash from weak explosive activity at Etna in 2006 and the 2007 eruptive crisis at Stromboli. Physics and Chemistry of the Earth, Parts A/B/C, 45-46, 113–127. doi:10.1016/j.pce.2011.02.001

Lautze, N. C., & Houghton, B. F. (2008). Single explosions at Stromboli in 2002: Use of clast microtextures to map physical diversity across a fragmentation zone. Journal of Volcanology and Geothermal Research, 170(3-4), 262–268. doi:10.1016/j.jvolgeores.2007.10.011

Lautze, N.C., Houghton, B.F. (2007). Linking variable explosion style and magma textures during 2002 at Stromboli volcano, Italy. Bull. Volcanol. 69, 445–460. doi:10.1007/s00445-006-0086-1

Lautze, N.C., Houghton, B.F. (2005). Physical mingling of magma and complex eruption dynamics in the shallow conduit at Stromboli volcano, Italy. Geology 33, 425–428. doi:10.1130/G21325.1

Leduc, L., Gurioli, L., Harris, A., Colò, L., & Rose-Koga, E. F. (2015). Types and mechanisms of strombolian explosions: characterization of a gas-dominated explosion at Stromboli. Bulletin of Volcanology, 77(1). doi:10.1007/s00445-014-0888-5

Leibrandt, S., and Le Pennec, J.-L. (2015). Towards fast and routine analyses of volcanic ash morphometry for eruption surveillance applications. Journal of Volcanology and Geothermal Research, 297, 11–27. https://doi.org/10.1016/j.jvolgeores.2015.03.014

Mercalli, G. (1907). Vulcani Attivi della Terra Morfologia—Dinamismo—Prodotti Distribuzione Geografica-Cause. Nature, 76(1969), 291–291. doi:10.1038/076291a0

Métrich, N. (2005). Triggering mechanism at the origin of paroxysms at Stromboli (Aeolian Archipelago, Italy): The 5 April 2003 eruption. Geophysical Research Letters, 32(10). doi:10.1029/2004gl022257

Nave, R., Isaia, R., Vilardo, G., & Barclay, J. (2010). Re-assessing volcanic hazard maps for improving volcanic risk communication: application to Stromboli Island, Italy. Journal of Maps, 6(1), 260–269. doi:10.4113/jom.2010.1061

Ntepe, N., & Dorel, J. (1990). Observations of seismic volcanic signals at stromboli volcano (Italy). Journal of Volcanology and Geothermal Research, 43(1-4), 235–251. doi:10.1016/0377-0273(90)90054-j

Oppenheimer, J., Capponi, A., Cashman, K. V., Lane, S.J., Rust, A.C., James, M.R. (2020). Analogue experiments on the rise of large bubbles through a solids-rich suspension: A “weak plug” model for Strombolian eruptions. Earth Planet. Sci. Lett. 531, 115931. doi:10.1016/j.epsl.2019.115931

Parfitt, E. A., & Wilson, L. (1995). Explosive volcanic eruptions-IX. The transition between Hawaiian-style lava fountaining and Strombolian explosive activity. Geophysical Journal International, 121(1), 226–232. doi:10.1111/j.1365-246x.1995.tb03523.x

Patrick, M. R., Harris, A. J. L., Ripepe, M., Dehn, J., Rothery, D. A., & Calvari, S. (2007). Strombolian explosive styles and source conditions: insights from thermal (FLIR) video. Bulletin of Volcanology, 69(7), 769–784. doi:10.1007/s00445-006-0107-0

Pering, T.D., Liu, E.J., Wood, K., Wilkes, T.C., Aiuppa, A., Tamburello, G., Bitetto, M., Richardson, T., & McGonigle, A.J.S. (2020). Combined ground and aerial measurements resolve vent-specific gas fluxes from a multi-vent volcano. Nat Commun 11, 3039 (2020). doi:10.1038/s41467-020-16862-w

Pering, T.D., McGonigle, A.J.S., James, M.R., Tamburello, G., Aiuppa, A., Delle Donne, D., Ripepe, M., 2016. Conduit dynamics and post explosion degassing on Stromboli: A combined UV camera and numerical modeling treatment. Geophys. Res. Lett. 43, 5009–5016. https://doi.org/10.1002/2016GL069001

Pioli, L., & Harris, A. J. L. (2019). Real-Time Geophysical Monitoring of Particle Size Distribution During Volcanic Explosions at Stromboli Volcano (Italy). Frontiers in Earth Science, 7. doi:10.3389/feart.2019.00052

Pioli, L., Pistolesi, M., & Rosi, M. (2014). Transient explosions at open-vent volcanoes: The case of Stromboli (Italy). Geology, 42(10), 863–866. doi:10.1130/g35844.1

Platt, U., Stutz, J. (2008). Differential Optical Absorption Spectroscopy. Physics of Earth and Space Environments. doi:10.1007/978-3-540-75776-4

Ripepe, M., Delle Donne, D., Lacanna, G., Marchetti, E., & Ulivieri, G. (2009). The onset of the 2007 Stromboli effusive eruption recorded by an integrated geophysical network. Journal of Volcanology and Geothermal Research, 182(3-4), 131–136. doi:10.1016/j.jvolgeores.2009.02.011

Ripepe, M., Donne, D. D., Harris, A., Marchetti, E., & Ulivieri, G. (2008). Dynamics of Strombolian Activity. Geophysical Monograph Series, 39–48. doi:10.1029/182gm05

Ripepe, M., Marchetti, E., & Ulivieri, G. (2007). Infrasonic monitoring at Stromboli volcano during the 2003 effusive eruption: Insights on the explosive and degassing process of an open conduit system. Journal of Geophysical Research, 112(B9). doi:10.1029/2006jb004613

Ripepe, M., Marchetti, E., Ulivieri, G., Harris, A., Dehn, J., Burton, M., … Salerno, G. (2005). Effusive to explosive transition during the 2003 eruption of Stromboli volcano. Geology, 33(5), 341. doi:10.1130/g21173.1

Ripepe, M., Harris, A. J. L., & Carniel, R. (2002). Thermal, seismic and infrasonic evidences of variable degassing rates at Stromboli volcano. Journal of Volcanology and Geothermal Research, 118(3-4), 285–297. doi:10.1016/s0377-0273(02)00298-6

Ripepe, M., Ciliberto, S., & Della Schiava, M. (2001). Time constraints for modeling source dynamics of volcanic explosions at Stromboli. Journal of Geophysical Research: Solid Earth, 106(B5), 8713–8727. doi:10.1029/2000jb900374

Ripepe, M., & Gordeev, E. (1999). Gas bubble dynamics model for shallow volcanic tremor at Stromboli. Journal of Geophysical Research: Solid Earth, 104(B5), 10639–10654. doi:10.1029/98jb02734

Ripepe, M., Rossi, M., & Saccorotti, G. (1993). Image processing of explosive activity at Stromboli. Journal of Volcanology and Geothermal Research, 54(3-4), 335–351. doi:10.1016/0377-0273(93)90071-x

Rosi, M., Pistolesi, M., Bertagnini, A., Landi, P., Pompilio, M., & Di Roberto, A. (2013). Chapter 14 Stromboli volcano, Aeolian Islands (Italy): present eruptive activity and hazards. Geological Society, London, Memoirs, 37(1), 473–490. doi:10.1144/m37.14

Rosi, M., Bertagnini, A., & Landi, P. (2000). Onset of the persistent activity at Stromboli Volcano (Italy). Bulletin of Volcanology, 62(4-5), 294–300. doi:10.1007/s004450000098

Schmid, R. (1981). Descriptive nomenclature and classification of pyroclastic deposits and fragments. Geologische Rundschau, 70(2), 794–799. doi:10.1007/bf01822152

Simons, B. C., Cronin, S. J., Eccles, J. D., Bebbington, M. S., & Jolly, A. D. (2020a). Spatiotemporal variations in eruption style, magnitude and vent morphology at Yasur volcano, Vanuatu: insights into the conduit system. Bulletin of Volcanology, 82(8). doi:10.1007/s00445-020-01394-4

Simons, B. C., S. J. Cronin, J. D. Eccles, A. D. Jolly, E. Garaebiti & S. Cevuard (2020b) Spatiotemporal variations in eruption style and magnitude at Yasur volcano, Vanuatu: Part 2. Extending Strombolian eruption classifications. Bulletin of Volcanology 82. In press

Slawson, P. R., & Csanady, G. T. (1967). On the mean path of buoyant, bent-over chimney plumes. Journal of Fluid Mechanics, 28(02), 311. doi:10.1017/s0022112067002095

Smekens, J.-F., Burton, M. R., & Clarke, A. B. (2015). Validation of the SO 2 camera for high temporal and spatial resolution monitoring of SO 2 emissions. Journal of Volcanology and Geothermal Research, 300, 37–47. doi:10.1016/j.jvolgeores.2014.10.014

Suckale, J., Keller, T., Cashman, K. V., Persson, P.O. (2016). Flow-to-fracture transition in a volcanic mush plug may govern normal eruptions at Stromboli. Geophys. Res. Lett. 43, 12,071-12,081. doi:10.1002/2016GL071501

Taddeucci, J., Edmonds, M., Houghton, B., James, M. R., & Vergniolle, S. (2015). Hawaiian and Strombolian eruptions. In The encyclopedia of volcanoes (pp. 485-503). Academic Press. doi:10.1016/B978-0-12-385938-9.00027-4

Taddeucci, J., Scarlato, P., Capponi, A., Del Bello, E., Cimarelli, C., Palladino, D. M., & Kueppers, U. (2012). High-speed imaging of Strombolian explosions: The ejection velocity of pyroclasts. Geophysical Research Letters, 39(2). doi:10.1029/2011gl050404

Tamburello, G., Aiuppa, A., Kantzas, E. P., McGonigle, A. J. S., & Ripepe, M. (2012). Passive vs. active degassing modes at an open-vent volcano (Stromboli, Italy). Earth and Planetary Science Letters, 359-360, 106–116. doi:10.1016/j.epsl.2012.09.050

Thivet, S., Gurioli, L., Di Muro, A., Derrien, A., Ferrazzini, V., Gouhier, M., Coppola, D., Galle, B., and Arellano, S. (2020a). Evidences of plug pressurization enhancing magma fragmentation during the September 2016 basaltic eruption at Piton de la Fournaise (La Réunion Island, France). Geochemistry, Geophysics, Geosystems, 21, e2019GC008611. https://doi.org/10.1029/2019GC008611

Thivet, S., Gurioli, L., Di Muro, A., Eychenne, J., Besson, P., and Nedelec J.-M., (2020b). Variability of ash deposits at Piton de la Fournaise (La Reunion Island): insights into fragmentation processes at basaltic shield volcanoes. Bulletin of Volcanology, doi:10.1007/s00445-020-01398-0

Turner, J. S. (1969). Buoyant Plumes and Thermals. Annual Review of Fluid Mechanics, 1(1), 29–44. doi:10.1146/annurev.fl.01.010169.000333

Turner, J. S. (1962). The “starting plume” in neutral surroundings. Journal of Fluid Mechanics, 13(03), 356. doi:10.1017/s0022112062000762

Valade, S., Lacanna, G., Coppola, D., Laiolo, M., Pistolesi, M., Donne, D. D., … Ripepe, M. (2016). Tracking dynamics of magma migration in open-conduit systems. Bulletin of Volcanology, 78(11). doi:10.1007/s00445-016-1072-x

Vergniolle, S., Boichu, M., & Caplan-Auerbach, J. (2004). Acoustic measurements of the 1999 basaltic eruption of Shishaldin volcano, Alaska. Journal of Volcanology and Geothermal Research, 137(1-3), 109–134. doi:10.1016/j.jvolgeores.2004.05.003

Vergniolle, S., & Brandeis, G. (1996). Strombolian explosions: 1. A large bubble breaking at the surface of a lava column as a source of sound. Journal of Geophysical Research: Solid Earth, 101(B9), 20433–20447. doi:10.1029/96jb01178

Vergniolle, S., & Brandeis, G. (1994). Origin of the sound generated by Strombolian explosions. Geophysical Research Letters, 21(18), 1959–1962. doi:10.1029/94gl01286

Voigt, S., Orphal, J., Bogumil, K., & Burrows, J. P. (2001). The temperature dependence (203–293 K) of the absorption cross sections of O3 in the 230–850 nm region measured by Fourier-transform spectroscopy. Journal of Photochemistry and Photobiology A: Chemistry, 143(1), 1–9. doi:10.1016/s1010-6030(01)00480-4

Washington, H. S. (1917). Persistence of vents at Stromboli and its bearing on volcanic mechanism. Geological Society of America Bulletin, 28(1), 249–278. doi:10.1130/gsab-28-249

Weill, A., Brandeis, G., Vergniolle, S., Baudin, F., Bilbille, J., Fèvre, J.-F., … Hill, X. (1992). Acoustic sounder measurements of the vertical velocity of volcanic jets at Stromboli Volcano. Geophysical Research Letters, 19(23), 2357–2360. doi:10.1029/92gl02502

Williams-Jones, G., Horton, K. A., Elias, T., Garbeil, H., Mouginis-Mark, P. J., Sutton, A. J., & Harris, A. J. (2006). Accurately measuring volcanic plume velocity with multiple UV spectrometers. Bulletin of Volcanology, 68(4), 328-332. doi:10.1007/s00445-005-0013-x